ARCHIVES OF ELECTRICAL ENGINEERING VOL. 74(1), pp. 151 –163 (2025)

DOI 10.24425/aee.2025.153017

Coil-based high-frequency modeling of permanent magnet synchronous machines with single-tooth windings

HUJUN PENG ✉, YUE YU, SVETOMIR STEVIC, SEBASTIAN MÖNNINGHOFF, KAY HAMEYER

Institute of Electrical Machines, RWTH Aachen University
Schinkelstr. 4, 52062 Aachen, German

e-mail: {✉ hujun.peng/hameyer/yue.yu/svetomir.stevic/sebastian.moenninghoff}@iem.rwth-aachen.de

(Received: 01.09.2024, revised: 10.02.2025)

Abstract: This paper presents a coil-based model for a permanent magnet synchronous machine (PMSM) with single-tooth windings to analyze the voltage distribution along its stator winding. The model encompasses considerations for the skin effect, the proximity effect of the winding, and parasitic capacitance within the machine. The model is parameterized using impedance measurement results. Subsequently, it undergoes validation in both the frequency and time domains. In the frequency domain, validation is carried out by comparing the measured and simulated impedance spectra. In the time domain, voltage and current signals are recorded from an operating machine on the test bench. The modeled and measured voltage and current signals during switching processes of power electronic devices are compared for validation in the time domain.

Key words: high-frequency modeling, PMSM, single-tooth winding, transient voltage

1. Introduction

The PMSM finds widespread application in the automotive industry and electrical aircraft owing to its compact size, high power density, and favorable mechanical characteristics [1]. To further enhance the power density of PMSMs, adopting single-tooth windings with a high copper factor is a common design choice, capable of improving the efficiency and power density of the electrical machine [2]. However, the configuration of single-tooth windings can lead to high voltage and current harmonics [9], especially when incorporating wide-gap semiconductors such

as SiC and GaN-Based MOSFETs. These devices offer high switching frequency and voltage slew rate compared to insulated-gate bipolar transistors (IGBTs) [8], resulting in increased voltage oscillation at winding terminals and along the winding [3]. Consequently, challenges related to insulation failure caused by overvoltage and achieving uniform voltage distribution must be carefully addressed in application scenarios [4]. In this regard, estimating electric stress is essential, for instance, through the design of insulation systems and fault diagnosis of electric devices.

The so-called high-frequency model is a universal tool to estimate the overvoltage by transient behaviors of electrical machines [10]. And the grey-box modeling is a commonly used method in the high-frequency modeling of electric machines. It combines the structural information of the electric machine with EMI-related measurements for modeling. Compared to white-box modeling, which requires detailed geometrical and material information of the components [12], the grey-box model offers advantages in terms of speed, simplicity, and lower computational requirements. An example of the grey-box model is provided by researchers in [5] to predict the voltage distribution along the stator winding. However, this study does not account for the proximity and skin effects. In [6], the state-of-the-art of this approach is presented, addressing these limitations by modeling electromagnetic coupling within a PMSM with hairpin winding, leveraging its symmetrical winding structure. Additionally, the research in [7] offers a turn-based grey-box model for a single tooth winding. However, no grey-box model for an entire stator winding has been validated with loading machines on a test bench yet.

In contrast to existing research, this study aims to determine the voltage distribution along the stator winding using a grey-box model based on winding structure and impedance measurement, rather than a white-box model based on finite element analysis. The subsequent sections introduce the measurement setup, modeling principle, and model validation in both frequency and time domains.

2. Measurement and modeling setup

Figure 1 illustrates the internal structure of the PMSM stator winding. The stator comprises 24 slots, each housing a tooth winding. The machine features eight pole pairs. Each phase consists of four parallel branches with two coils interconnected in series. Additionally, four separate neutral points are not connected.

Figure 2 depicts the setup for impedance measurement. A DC current source is applied to adjust the rotor position of the PMSM before measurement to ensure its consistency during the measurement phase.

The impedance spectra are primarily measured across three distinct categories of topologies, as outlined in Table 1. The corresponding results are presented in Fig. 3.

The measurement results demonstrate relatively significant similarity between phases U, V, and W. It is noted that the impedance spectra of topologies within the same category are a little different. Through additional measurement rounds, it has been observed that the impedance spectra vary with different rotor positions. Previous research has suggested that the impact of rotor positions on characteristics in the high-frequency range is not significant [11]. Therefore, this study does not consider the impedance change resulting from rotor positions. The modeling in the frequency domain is based on the measurement round illustrated in Fig. 3.

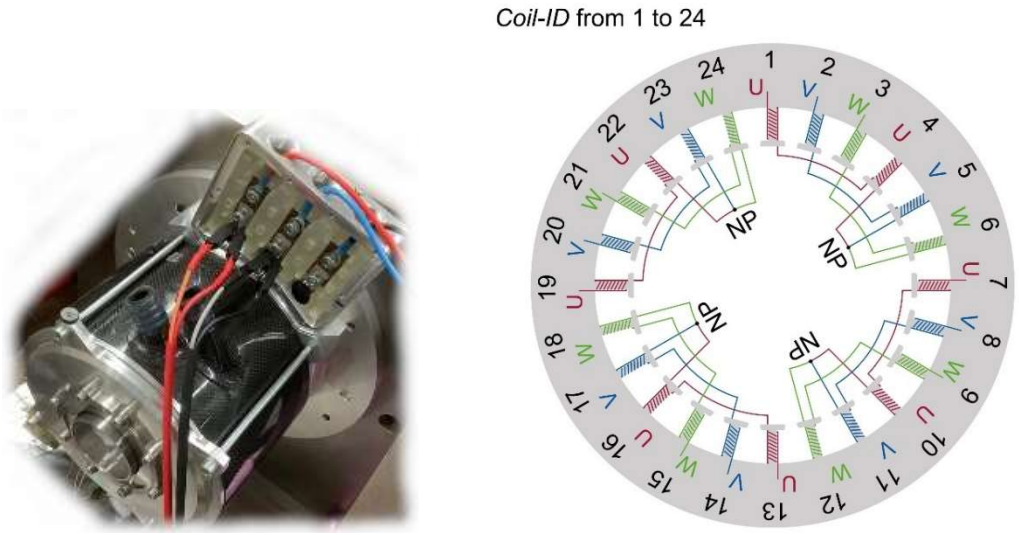

(a) (b)

Fig. 1. The modeled PMSM: the modeled PMSM by impedance measurement (a); structure of the stator winding (b)

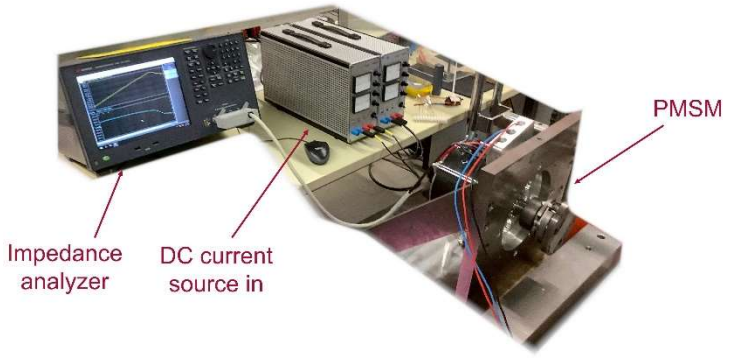

Fig. 2. Setup of PMSM impedance measurement

Table 1. Summary of the impedance measurement topologies of the PMSM

Category	Topologies	Descriptions
Phase-to-GND	*U-to-GND*, *V-to-GND*, *W-to-GND*	Impedance between one phase and machine housing
Phase-to-Phase	*U-to-V*, *V-to-W*, *W-to-U*	Impedance between one phase and another phase
Phase-to-Phases	*U-to-VW*, *V-to-WU*, *W-to-UV*	Impedance between one phase and the other phases

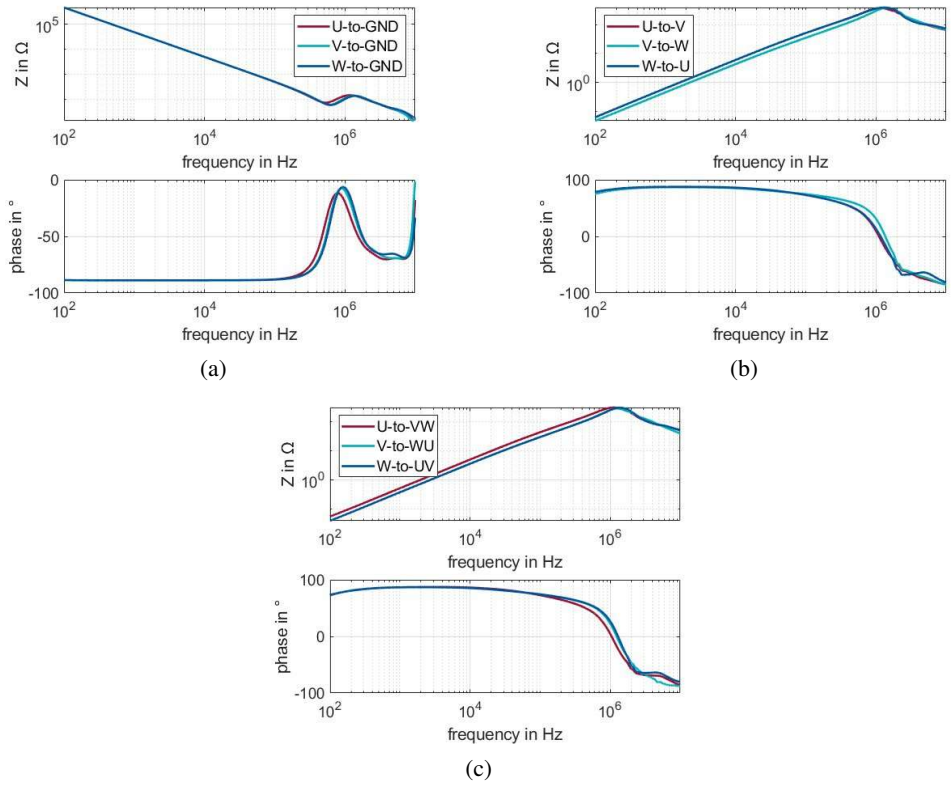

Fig. 3. Measured impedance spectra for different terminal configurations of the PMSM: topologies 'Phase-to-GND' (a); topologies 'Phase-to-Phase' (b); topologies 'Phase-to-Phases' (c)

After analyzing impedance measurements below 10 kHz, it is observed that differential mode (DM) impedances (categories 'Phase-to-Phase' and 'Phase-to-Phases') demonstrate an inductive behavior within the stator. At the same time, common mode (CM) impedances (category 'Phase-to-GND') predominantly exhibit a capacitive behavior. Due to the skin and proximity effects, the DM-impedance amplitude increases with frequency. Upon surpassing the 1 MHz point, a profound decrease in phase within the DM impedance suggests capacitive coupling within the stator winding. These phenomena must be considered during the modeling process.

Each coil is individually modeled and then connected. The following frequency-dependent effects are considered in the model, as illustrated in Fig. 4:

– Capacitive coupling between coils and the machine housing,
– Capacitive coupling between neighboring coils and within each coil,
– Frequency-dependent losses due to polarization in dielectric,
– Proximity effects between neighboring coils and skin effect in each coil.

Figure 5 provides an overview of the winding model structure. Each coil is identified as the fundamental modeling unit, later interconnected according to the periodically repeated winding structure depicted in Fig. 1. In this context, indices indicate the geometric position of each coil. For instance, Coil_{i-1} represents the coil preceding Coil_i, while Coil_{i+1} represents the subsequent coil after Coil_i.

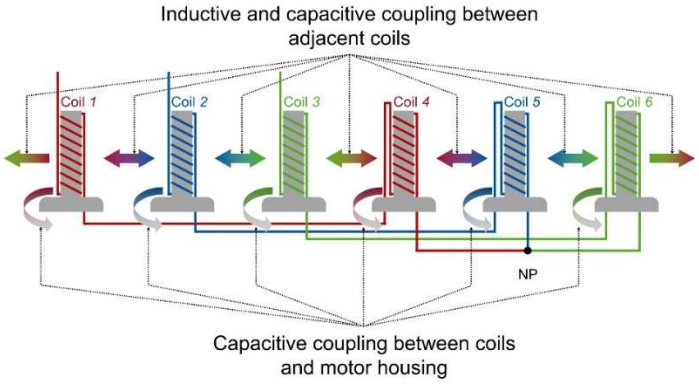

Fig. 4. Inductive and capacitive coupling between coils in the PMSM

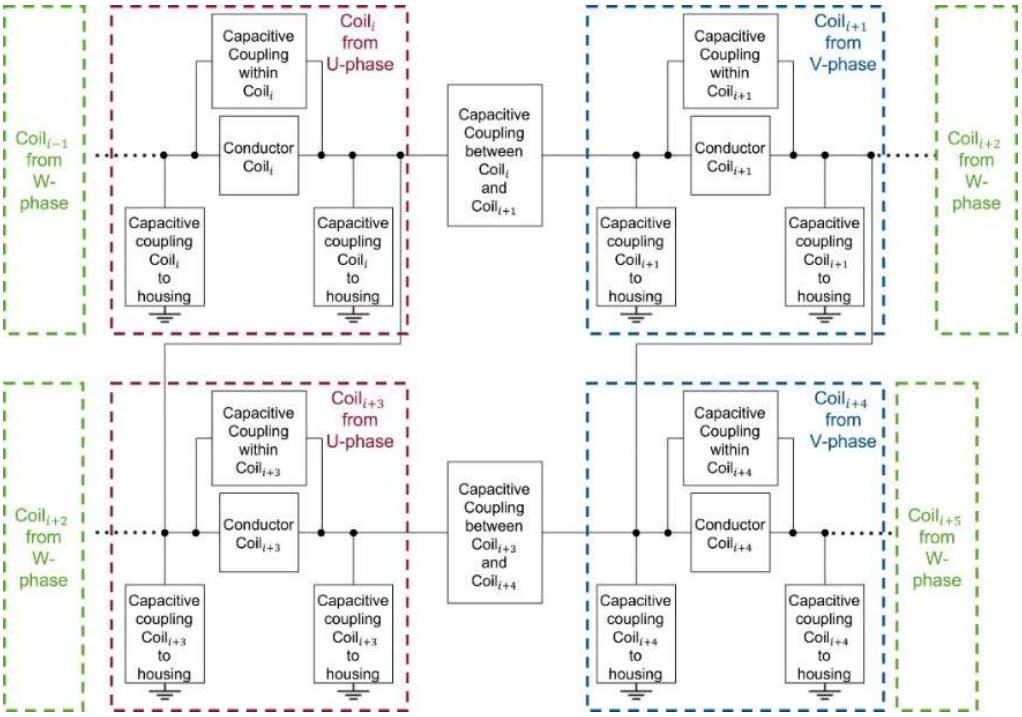

Fig. 5. Basic model unit structure of coils in the PMSM

Capacitive coupling is modeled using an equivalent circuit structure with two parallel branches, as shown in Fig. 6. The first branch, consisting solely of a capacitor, represents the internal parasitic capacitance within the stator winding. In this context, we disregard the parasitic capacitance between components that are spatially distant from one another, focusing only on the parasitic capacitance between adjacent coils and between each coil and the machine housing. However,

the effect of the dielectric medium, particularly at high frequencies, cannot be overlooked, as it contributes to dielectric loss within the electric machine. The increasing frequency of the varying electric field exacerbates this phenomenon [13]. To account for this, an additional branch, consisting of a resistor and a capacitor in series, is introduced to provide a simplified representation of the frequency-dependent dielectric loss. Additionally, a parallel resistor with a relatively high value is incorporated to model the behavior of the insulation layer, as illustrated in Fig. 6(b), where the machine housing is treated as the zero-potential point.

(a) (b)

Fig. 6. Model of capacitive coupling between: two neighbouring coils (a); stator winding and machine housing (b)

Figure 7 illustrates the model structure of each coil winding, divided into three segments. The first segment, labelled 'Part-A', employs the 'RL-Ladder' structure, a common approach to modeling the skin effect in conductors. In this case, variations in voltage distribution are mainly attributed to the self-induction of the conductor. Additionally, a single series resistor is included to represent potential frequency-independent characteristics or other uncertain effects of the winding in a simplified manner.

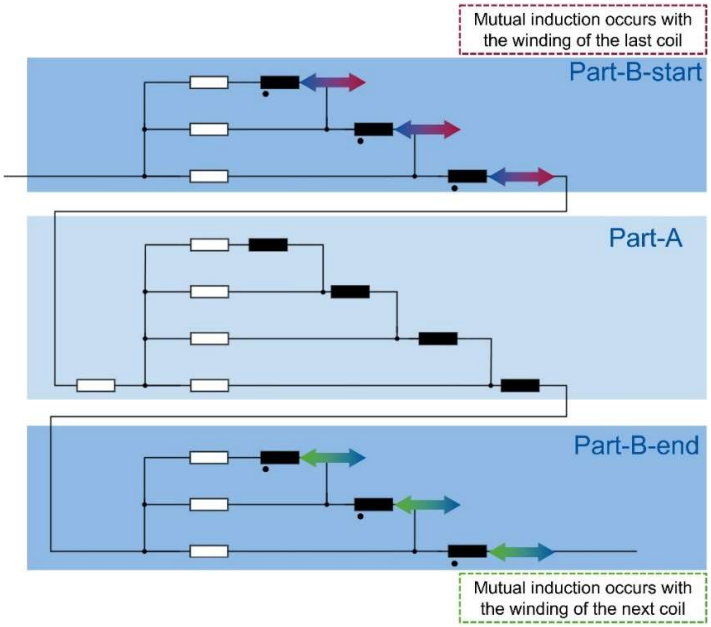

Fig. 7. Basic model unit structure of coils in the PMSM

For the remaining two segments, 'Part-B-start' and 'Part-B-end', the configuration incorporates an additional three RL-Ladder structures. The innovative aspect of this paper lies in the inclusion of mutual inductances across all corresponding RL layers, enabling accurate representation of the inductive coupling between closely spaced coils. Following the winding schema shown in Fig. 7, 'Part-B-start' simulates the mutual induction between the windings of the modeled coil and its preceding coil.

Conversely, 'Part-B-end' simulates the mutual induction between the windings of the modeled coil and its subsequent coil. This design, integrating both Parts A and B, facilitates relative decoupling between the skin and proximity effects. While both effects contribute to an increase in impedance with rising frequency, they arise from distinct causes. As a result, the model is more capable of capturing the high-frequency behavior of the PMSM.

3. Validation in the frequency and time domain

3.1. Validation in frequency domain

The model parameters are identified through an optimization process based on impedance spectrum measurements. Figure 8 compares the modeled impedance spectra to those measured. Figure 9 illustrates the statistical results of the impedance modeling, which is evaluated with the

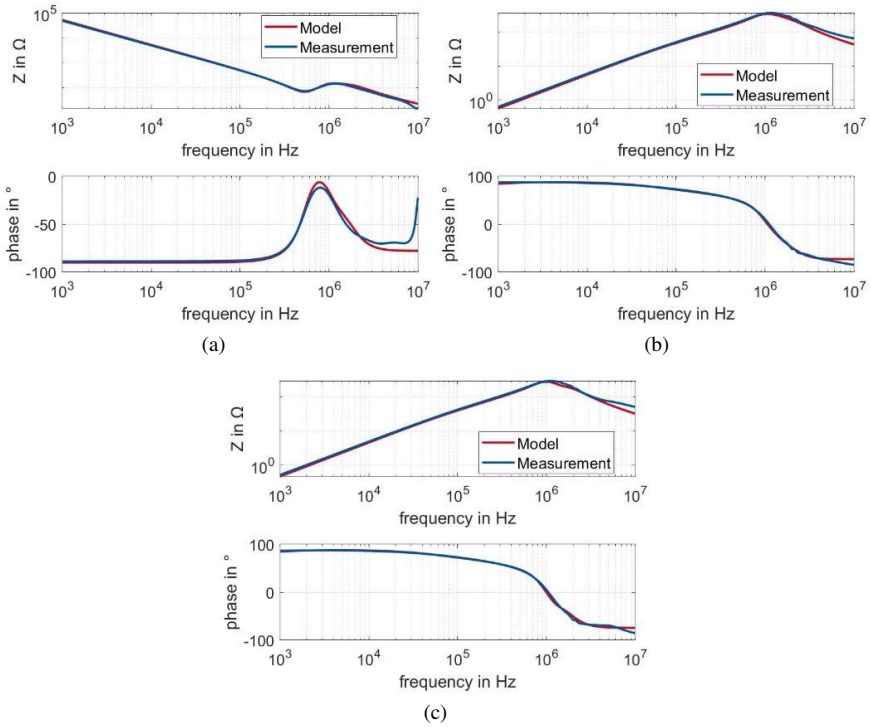

Fig. 8. Comparison between modeled and measured impedance spectra: topologies 'Phase-to-GND' (a); topologies 'Phase-to-Phase' (b); topologies 'Phase-to-Phases' (c)

so-called Mean Absolute Percentage Error (MAPE):

$$\text{MAPE} = \frac{100\%}{N} \sum_{i=1}^{N} \left| \frac{Z_i - \hat{Z}_i}{Z_i} \right|, \tag{1}$$

where:

Z_i is the measured impedance at frequency f_i,

$\hat{Z}_i$ is the modeled impedance at frequency f_i,

N is the sample size in frequency domain over impedance spectra from 1 kHz up to 10 MHz.

An average impedance error across all topologies from 1 kHz up to 10 MHz is achieved at 7.39%, as listed in Table 1. For all CM topologies, the average error is 7.80%, while the mean error is 7.18% for the DM topologies.

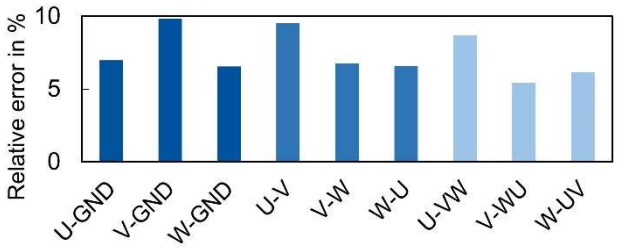

Fig. 9. Relative errors of the impedance modeling from 1 kHz to 10 MHz

3.2. Validation in time domain

Figure 10 illustrates the test bench used for time-domain validation. The PWM voltage generated by an inverter is fed into the PMSM through power cables. The current and voltage are measured at the inverter output, as depicted in Fig. 11. Besides the measurement on the test bench, a simulation model with a cable model connected with the PMSM model is established, as shown

Fig. 10. Configuration of the test bench for the time-domain validation

in Fig. 11. The phase-to-housing voltage signals at the inverter output are employed as inputs for the simulation – Fig. 12. Two kinds of signals are chosen for validation in the time domain:

a) $U_{u-to-housing}$: The voltage signal between U-terminal and housing of the PMSM,

b) I_{CM}: The common mode current at the inverter output.

A comparison between the measured signal and the corresponding simulated signal is given for validation.

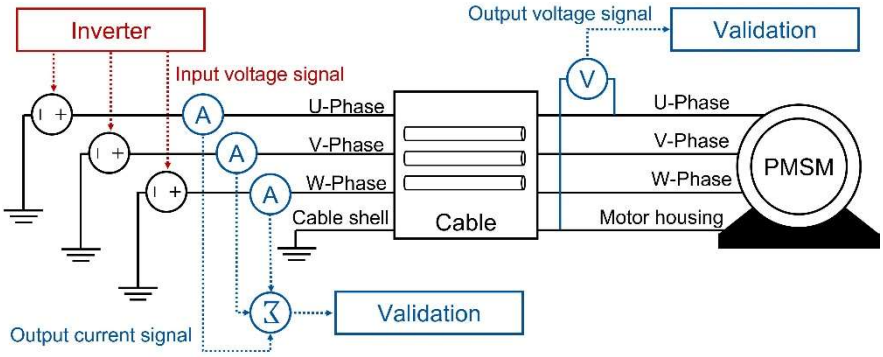

Fig. 11. Schematic configuration of the electric drive for simulation

Fig. 12. Phase-to-housing voltage and common mode current measurement within the inverter box

The original current and voltage signals are sampled at intervals of 0.4 ns. Low-pass filtering is essential before using the sampled signals. This processing is applied to all current and voltage signals. The validation is conducted with the PMSM operating at various speeds and switching frequencies. Figure 13 presents example results of validation based on measurements.

Figure 14 shows the statistics during validation using the measurement signals in time domain. Hereby, the relative error in the peak values of the voltage $U_{u-to-housing}$ and the common mode current I_{CM} before damping occur, is calculated as follows:

$$\Delta = 100\% \left| \frac{x - \hat{x}}{x} \right|, \tag{2}$$

where:

x: represents the peak value of measured signal of $U_{u-to-housing}$ and I_{CM},

$\hat{x}$: represents the peak value of modeled signal of $U_{u-to-housing}$ and I_{CM}.

In order to evaluate the transient behavior encountered, the first oscillation cycle after the peak is used as the natural oscillation period, to calculate the relative error in the oscillation frequency in the current and voltage signals:

$$\Delta_{\text{osc}} = 100\% \left| \frac{f_{\text{osc}} - \hat{f}_{\text{osc}}}{f_{\text{osc}}} \right|, \tag{3}$$

where:

f_{osc}: oscillation frequency of measured voltage and current signals during transient,

$\hat{f}_{\text{osc}}$: oscillation frequency of modeled voltage and current signals during transient.

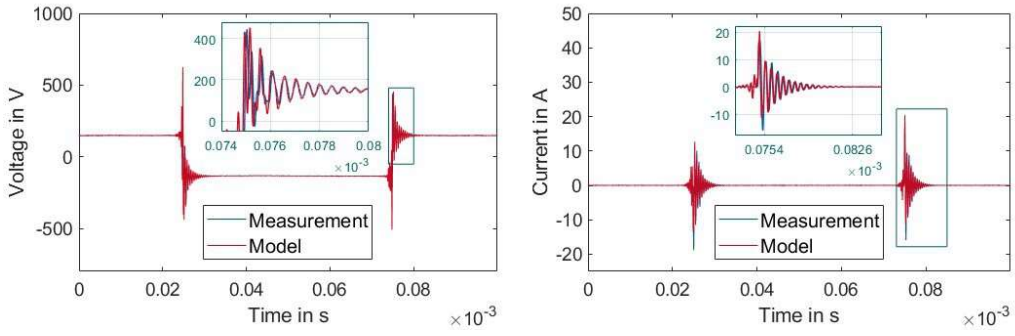

(a) (b)

Fig. 13. Resultls of time domain validation at at torque 0 Nm, motor speed 10 rpm and switching frequency 10 kHz: using $U_{u-to-housing}$ voltage (a); using common mode current (b)

The average relative error of the $U_{u-to-housing}$ at a motor speed of 10 rpm and zero torque is 7.41% for the voltage peak value and 1.57% for its oscillation frequency. Moreover, the average relative error of the common mode current I_{CM} at this motor speed and torque is 18.08% for the current peak value and 3.69% for its oscillation frequency.

At motor speed 500 rpm and zero torque, the average relative error of the $U_{u-to-housing}$ is 8.01% for the voltage peak value and 1.76% for its oscillation frequency. The average relative error of the I_{CM} at is 6.98% for the peak value and 2.23% for the oscillation frequency. At a motor speed of 5000 rpm, the average relative error of the $U_{u-to-housing}$ is 4.82% for the voltage peak value and 2.80% for its oscillation frequency. The average relative error of the I_{CM} is 4.32% for the peak value and 2.34% for its oscillation frequency.

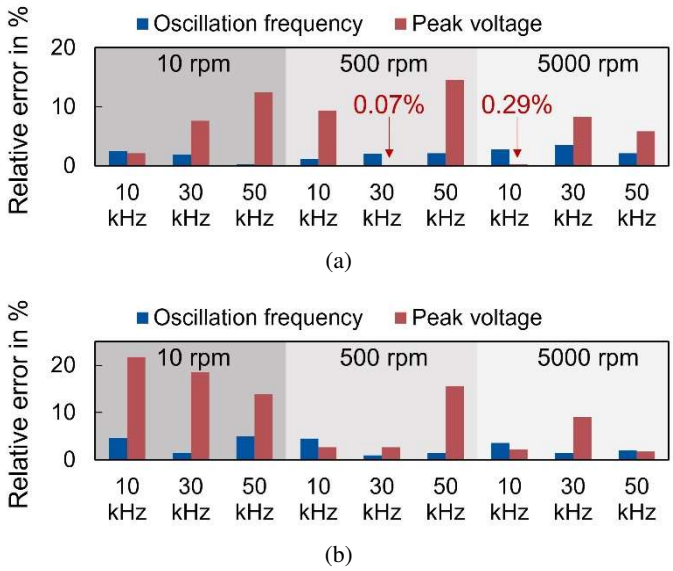

Fig. 14. Statistic of validation results at torque 0 Nm and different rotor speeds: using $U_{u-to-housing}$ voltage (a); using common mode current (b)

The model exhibits high accuracy in predicting the transition of oscillation frequency, with an overall deviation under 3%. In contrast to the oscillation frequency, the deviations of the peak values at certain operating points are relatively high. This discrepancy is primarily attributed to the inaccuracy of the cable model. The position and environment during measuring the cables for impedance modeling differ from the environment on the test bench in Fig. 10.

Further measurements with a three-phase cable set confirmed this hypothesis. The cable connection scheme during impedance measurement is shown in Fig. 15. In the physical setup in Fig. 16(a), the two ends of the three cables are respectively short-circuited together, and the impedance between one port of the cables and the cable shell is measured twice: once in a straight layout and once in a coiled layout. Figure 16(b). depicts the measurement results, revealing that different geometric layouts significantly impact the impedance spectra of the cable above 1 MHz, consequently affecting the transient behavior of the current and voltage signals during the switching processes of power electronic devices.

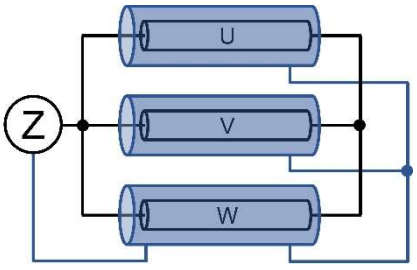

Fig. 15. Configuration topology for impedance measurement of the cables

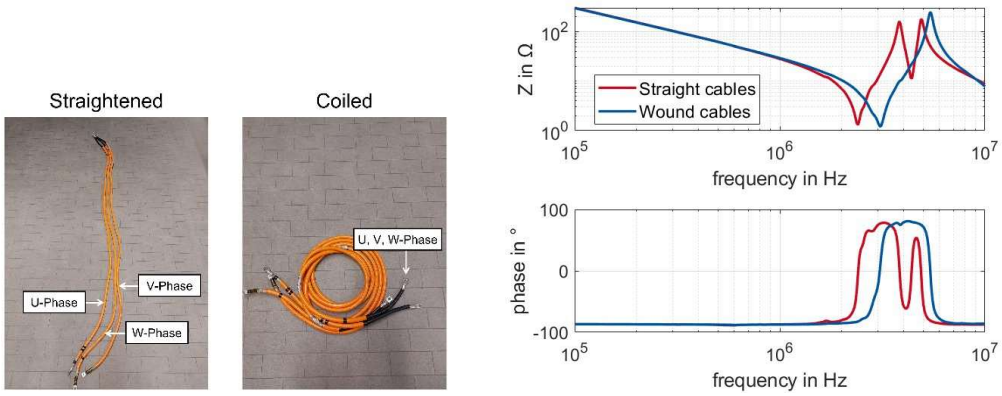

(a) (b)

Fig. 16. Cable set in various layout: various geometrical layout (a); impedance spectra of various geometrical layout (b)

4. Conclusions

In this research, the proposed 'coil-based' PMSM model demonstrates high accuracy in both the frequency and time domains. A key contribution is its ability to model the frequency-dependent proximity effect between windings of different coils, in addition to the skin effect. This model enables the calculation of voltage distribution along the stator winding, showcasing its potential for practical applications such as fault detection and insulation system design. It also provides a foundation for more detailed modeling in future research studies. Further work will aim to enhance the high-frequency model by incorporating the influence of the operating environment.

References

[1] Liu C., Chau K.T., Lee C.H., Song Z., *A critical review of advanced electric machines and control strategies for electric vehicles*, Proceedings of the IEEE, vol. 109, no. 6, pp. 1004–1028 (2020), DOI: 10.1109/JPROC.2020.3041417.

[2] Deshpande Y.B., Toliyat H.A., Nair S.S., Dhinagar S.J., Immadisetty S., Nalakath S., *High-torque-density single tooth-wound bar conductor permanent-magnet motor for electric two-wheeler application*, IEEE Transactions on Industry Applications, vol. 51, no. 3, pp. 2123–2135 (2014), DOI: 10.1109/TIA.2014.2369822.

[3] Wang Y., Lyu G., Wei J., Zheng Z., He J., Lei J., Chen K.J., *Characterization of static and dynamic behavior of 1200 V normally off GaN/SiC cascode devices*, IEEE Transactions on Industrial Electronics, vol. 67, no. 12, pp. 10284–10294 (2019), DOI: 10.1109/TIE.2019.2959512.

[4] Lee H., Smet V., Tummala R., *A review of SiC power module packaging technologies: challenges, advances, and emerging issues*, IEEE Journal of Emerging and Selected Topics in Power Electronics, vol. 8, no. 1, pp. 239–255 (2019), DOI: 10.1109/JESTPE.2019.2951801.

[5] Zheng D., Lu G., Zhang P., *An improved online stator insulation monitoring method based on common-mode impedance spectrum considering the effect of aging position*, IEEE Transactions on Industry Applications, vol. 58, no. 3, pp. 3558–3566 (2022), DOI: 10.1109/TIA.2022.3160131.

[6] Peng H., Stevic S., Luo Z., Driendl N., Butterweck D., Sharifian L., Firouz Y., Hameyer K., *Voltage distribution modeling along stator windings in permanent magnet synchronous machines using coil-based grey box models*, IEEE Transactions on Energy Conversion, vol. 39, no. 3, pp. 1994–2007 (2024), DOI: 10.1109/TEC.2024.3370800.

[7] Peng H., Yu Y., Hameyer K., *Conductor-based modeling of a single-tooth winding for EMI simulation*, IEEE Transactions on Power Electronics, vol. 39, no. 9, pp. 11099–11109 (2024), DOI: 10.1109/TPEL.2024.3403669.

[8] Kono H. *et al*., *Improving the specific on-resistance and short-circuit ruggedness tradeoff of 1.2-kV-class SBD-embedded SiC MOSFETs through cell pitch reduction and internal resistance optimization*, 33rd International Symposium on Power Semiconductor Devices and ICs (ISPSD), Nagoya, Japan, pp. 227–230 (2021).

[9] Abdel-Khalik A.S., Diab M.S., Ahmed S., Massoud A.M., *A new single tooth winding layout for a single-phase induction motor with segmented stator*, 41st Annual Conference of the IEEE Industrial Electronics Society, Yokohama, Japan, pp. 000102–000107 (2015).

[10] Ruiz-Sarrió J.E., Chauvicourt F., Gyselinck J., Martis C., *High-Frequency Modelling of Electrical Machine Windings Using Numerical Methods*, 2021 IEEE International Electric Machines & Drives Conference (IEMDC), Hartford, CT, USA, pp. 1–7 (2021).

[11] Peng H., Driendl N., Stevic S., Sharifian L., Friouz Y., Butterweck D., Hameyer K., *A Study about the Influence of Rotor Position of IPMSM on the Maximum Voltage on Motor Terminals under Inverter-fed Operation*, 2023 IEEE 6th Student Conference on Electric Machines and Systems (SCEMS), Aachen, Germany, pp. 1–6 (2023).

[12] Stoll R., *The Analysis of Eddy Currents*, Clarendon Press (1974).

[13] von Hippel A.R., *Dielectric Materials and Applications*, Wiley (1954).